

# Following UV-induced electronic dynamics of thiouracil by ultrafast x-ray photoelectron spectroscopy

D. Mayer<sup>1+</sup>, F. Lever<sup>1+</sup>, D. Picconi<sup>2,\*</sup>, J. Metje<sup>1</sup>, S. Alisauskas<sup>3</sup>, F. Calegari<sup>4,5,6</sup>, S. Düsterer<sup>3</sup>, C. Ehler<sup>7</sup>, R. Feifel<sup>8</sup>, M. Niebuhr<sup>1</sup>, B. Manschwetus<sup>3</sup>, M. Kuhlmann<sup>3</sup>, T. Mazza<sup>9</sup>, M. S. Robinson<sup>1,4</sup>, R. J. Squibb<sup>8</sup>, A. Trabattoni<sup>4</sup>, M. Wallner<sup>8</sup>, P. Saalfrank<sup>2</sup>, T. J. A. Wolf<sup>10</sup> and M. Gühr<sup>1,\*</sup>

*1 Institut für Physik und Astronomie, Universität Potsdam, 14476 Potsdam Germany*

*2 Institut für Chemie, Universität Potsdam, 14476 Potsdam Germany*

*3 Deutsches Elektronen Synchrotron (DESY), 22607 Hamburg, Germany*

*4 Center for Free-Electron Laser Science (CFEL), DESY, 22607 Hamburg, Germany*

*5 The Hamburg Centre for Ultrafast Imaging, Universität Hamburg, 22761 Hamburg, Germany*

*6 Institut für Experimentalphysik, Universität Hamburg, 22761 Hamburg, Germany*

*7 Heidelberg Institute for Theoretical Studies, HITS gGmbH, 69118 Heidelberg, Germany*

*8 Department of Physics, University of Gothenburg, SE-41296 Gothenburg, Sweden*

*9 European XFEL, 22869 Schenefeld, Germany*

*10 Stanford PULSE Institute, SLAC National Accelerator Laboratory, 94025 Menlo Park, United States of America*

*+ Contributed equally*

*\* correspondence should be addressed to [david.picconi@uni-potsdam.de](mailto:david.picconi@uni-potsdam.de) and [mguehr@uni-potsdam.de](mailto:mguehr@uni-potsdam.de)*

## **Abstract**

Photoexcited molecules convert photon energy into other energetic degrees of freedom involving the coupling of ultrafast electronic and nuclear motion. Here, we demonstrate that time-resolved x-ray photoelectron spectroscopy (TR-XPS) offers a new way to investigate the molecular photoinduced dynamics based on changes in the local charge at the core-probed atom. The method shows strong sensitivity to electronic dynamics and, to a smaller extent, geometrical changes.

We demonstrate the power of TR-XPS by using sulphur 2p-core-electron-emission probing to study the UV-excited dynamics of 2-thiouracil. We identify the ultrafast Frank-Condon relaxation on the photoexcited  $S_2$  state. The majority of the photoexcited population relaxes to  $S_1$  and  $T_1$  states in accordance with the literature. In a second channel,  $\frac{1}{3}$  of the population relaxes to the molecular ground state within 200 fs. In addition, a 250-fs oscillation, visible in the kinetic energy of the TR-XPS, reveals a coherent exchange of population among electronic states.

## Introduction

Photoexcited molecules convert energy in the form of absorbed light into other energetic degrees of freedom via complex electronic-nuclear dynamics. While optical light directly couples to valence electrons, their rearrangement leads to a change in molecular geometry which can be predicted by propagating nuclear wave-packets on potential energy surfaces (PES) calculated within the Born-Oppenheimer Approximation (BOA). Energy conversion is however oftentimes decided at points in phase-space with energetically close PES (including conical intersections), where the BOA cannot be applied<sup>1</sup>. This complicates both the theoretical description and experimental observations due to the non-adiabatic couplings. Observables that rely on valence electron transitions have demonstrated ultrafast dynamics at these crucial points<sup>2,3</sup>, and both the electronic and nuclear dynamics shape the observables in a complicated and non-invertible way. Recent progress on time-resolved electron and x-ray diffraction provides direct observables of atom-pair distances with unprecedented insight on nuclear geometry changes<sup>4-9</sup>.

Ultrafast x-ray spectroscopy provides the advantage of probing the joint electronic and nuclear molecular dynamics with element- and site-specific responses<sup>10,11</sup>. X-ray absorption spectroscopy (XAS) in the hard x-ray range (several keV) is highly sensitive to charge and spin states<sup>12,13</sup>. In the soft x-ray range, absorption spectroscopy has the capability to monitor electronic and nuclear dynamics<sup>14-16</sup> which is demonstrated in ring opening<sup>17</sup>, dissociation<sup>18</sup>, intersystem-crossing<sup>19</sup>, ionization<sup>20</sup> as well as the interplay between  $\pi\pi^*$  and  $n\pi^*$  valence electronic states<sup>21,22</sup>. Compared to TR-XAS, time resolved x-ray photoelectron spectroscopy (TR-XPS) has the advantage that a fixed x-ray wavelength can be used to address several elements and sites. In addition, the use for molecules in thick solvent jets can also be accomplished employing harder x-rays for light-element photoemission. TR-XPS has been used to identify the states before and after the photodissociation process in a halogenated molecule<sup>23</sup> as well as in metal-centered compounds<sup>24</sup>. Theory predicts that TR-XPS should be useful for obtaining geometric as well as electronic information on molecular dynamics<sup>25-28</sup>.

In this paper, we now show that TR-XPS delivers element and site specific information of the electronic and nuclear dynamics. We furthermore deliver a very simple interpretation based on local charge at the probed atom being influenced by geometry and electronic state. The argument shows strong similarities to the classical interpretations in steady state spectroscopy<sup>29</sup> and will allow to circumvent complex calculations of ionization potentials (IPs), while allowing for an interpretation based on chemical intuition. We show that the largest effect on TR-XPS is due to electronic relaxation, especially if the local charge at the probed atom is grossly changed in the process. A smaller but non-negligible effect stems from geometry changes, which can also alter local charge at the probed atom. In our experiment, a UV pulse prepares 2-thiouracil in the optically active  $S_2$   $\pi\pi^*$  state and a time-delayed soft x-ray pulse is used to core-ionise the molecule via sulphur 2p photoemission (Fig. 1). The TR-XPS spectra are used to deduce the molecular dynamics using the concept stated above.

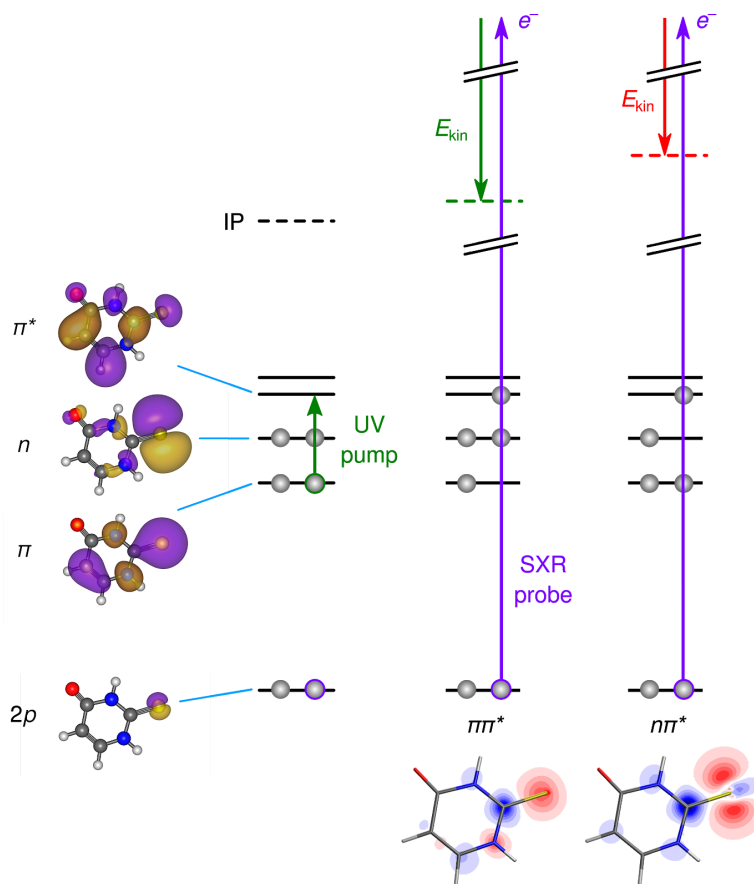
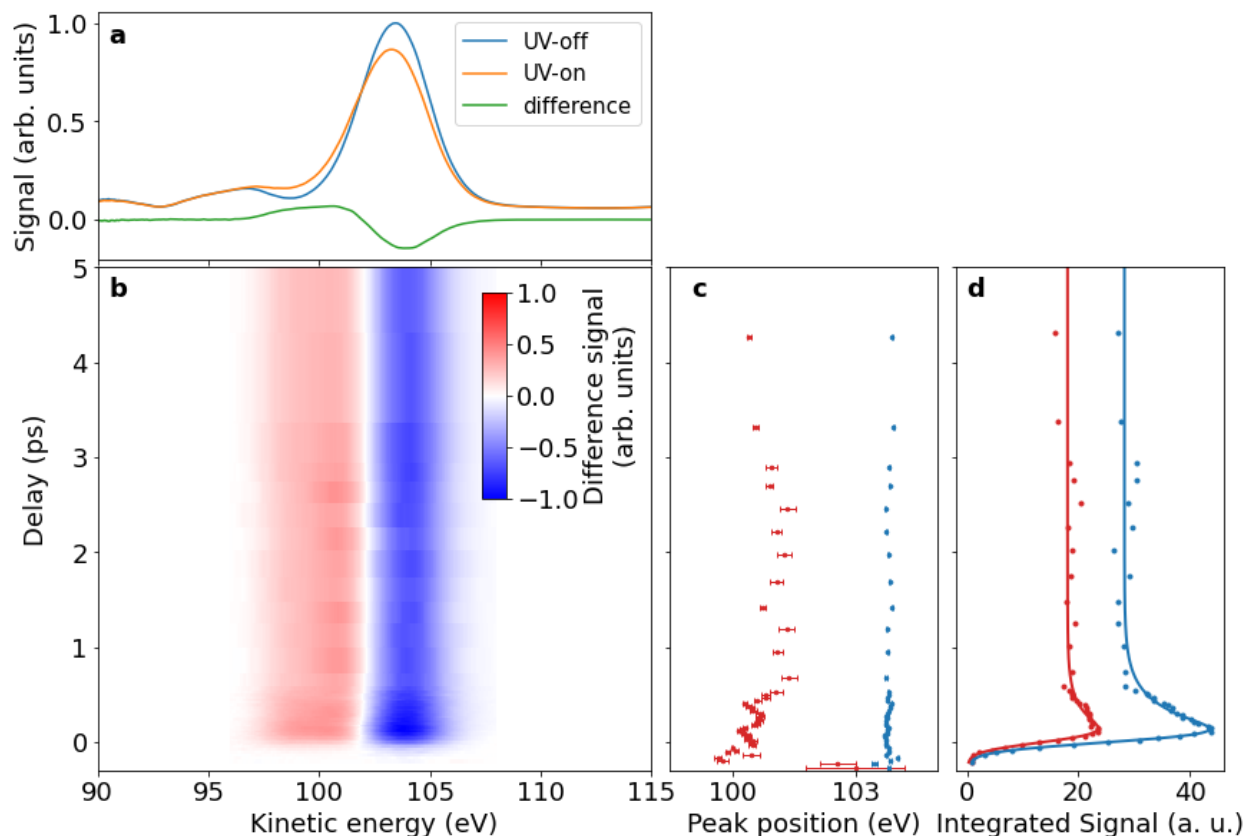


Figure 1: Schematic picture of the investigated process in a molecular orbital representation. A UV pump pulse (green arrow) excites the 2-thiouracil from its electronic ground state ( $S_0$ ) to a  $\pi\pi^*$  state ( $S_2$ ). A delayed soft x-ray probe pulse of 272 eV photon energy (purple arrow) accomplishes ionization of the sulphur 2p core level. The measured photoelectron kinetic energy is influenced by the local charge at the sulphur atom and therefore can track non-radiative transitions such as  $S_2 \pi\pi^* \rightarrow S_1 n\pi^*$ . The contour plots show the electron difference density for the  $\pi\pi^*$  and  $n\pi^*$  states, computed at the  $S_0$  minimum and integrated along the axis perpendicular to the molecular plane. The hole at the sulphur atom, depicted by the red contours, leads to a shift of the photoelectron spectrum to lower kinetic energies.

Photoexcited thionucleobases are interesting because of efficient relaxation into long lived triplet states (see Ref. <sup>30</sup> and references therein) triggering applications as photoinduced cross-linkers <sup>31,32</sup> and photoinduced cancer therapy <sup>33</sup>. Among those, 2-thiouracil is one of the most-studied on an ultrafast scale <sup>30</sup>, both experimentally, using transient absorption <sup>34</sup> and photoelectron spectroscopy <sup>34–36</sup>, and theoretically in static calculations <sup>37</sup> and surface hopping trajectory simulations <sup>38,39</sup>. The model emerging from joint experimental-theoretical investigations includes ultrafast internal conversion from the photoexcited  $S_2 \pi\pi^*$  state into the  $S_1 n\pi^*$  state, followed by a sub-picosecond intersystem crossing <sup>35</sup>. Relaxation from the triplet states to the ground state is observed with a time constant of several ten picoseconds <sup>35</sup>. While confirming the

$S_2$ - $S_1$ -triplet decay path, we also monitor an ultrafast ground state decay channel. Furthermore, we find an oscillation pattern in the difference spectrum, which we identify as coherent population exchange among different electronic states, as predicted by trajectory calculations<sup>38,39</sup>.

## Results



*Figure 2: Experimental time-resolved core-level photoelectron spectra of 2-thiouracil. (a) UV-off and UV-on photoelectron spectra as well as the difference spectrum between UV-on and UV-off. (b) False-colour plot of time-dependent difference PES with red indicating UV-induced increase of the photoelectron spectrum and blue a UV-induced decrease. (c) Changes in the spectral center of positive and negative contributions when fitted by two Gaussians. (d) Integrated Intensity of the positive and negative parts of the difference spectra (dots) and fit to the data (solid line).*

Figure 2a shows a photoelectron spectrum of 2-thiouracil obtained at a free-electron-laser (FEL) with a photon energy of 272 eV and an average bandwidth of 1-2 %. The electron spectra are taken with a magnetic-bottle electron spectrometer (MBES). We identify the sulphur 2p-photoline (blue) at an electron kinetic energy of 103.5 eV in agreement with the literature<sup>40</sup>. Unfortunately, the width of about 4 eV does not allow us to distinguish the spin-orbit splitting

<sup>40,41</sup>. The photoline is accompanied by a shake-up satellite at 96 eV <sup>42</sup>. Upon UV excitation (“UV-on”, orange line), the photoline shifts towards lower kinetic energies. The difference spectrum (“UV-on” - “UV-off”, green line) is equal to the difference between ground-state (GS) and excited-state (ES) spectra times the fraction  $f$  of excited molecules ( $f \cdot (ES - GS)$ ). Figure 2b shows a false-colour plot of the difference spectra. Temporal overlap has been determined by analysing the integrated absolute difference signal. Additionally, we fit the difference spectrum features to a superposition of a positive and negative Gaussian function, the centers of which are given in panel 2c. The area under the positive/negative lobe in the difference spectrum is given in 2d.

The difference feature keeps its characteristic lineshape over the timescale of our measurement, indicating a persistent kinetic energy shift to smaller values over the whole range. The difference-amplitude changes significantly during the first picosecond. We use an exponential model function convoluted with a Gaussian time-uncertainty function of 191 ( $\pm 11$ ) fs FWHM (see Supplementary Discussion 1). We observe an exponential decay of 247 ( $\pm 22$ ) fs to 75% signal for the negative part and 221 ( $\pm 38$ ) fs to 65% signal for the positive part. The positive amplitude is always smaller than the negative amplitude. Systematic investigations of the difference spectra for various experimental settings exhibit the influence of cyclotron resonances on the relative amplitudes in the MBES (see Supplementary Discussion 2). We therefore abstain from interpreting the relative strength of the positive and negative features.

On top of a 1 eV kinetic energy shift (Fig. 2c) on the positive lobe, we observe an oscillation with 250 fs period extending for about two periods. We cannot exclude that this beat continues, however after 800 fs the step size in the experiment is too coarse to make a statement about the oscillatory pattern.

In order to interpret the photoelectron signal we performed quantum chemical coupled-cluster calculations of the ground, valence-excited and core-ionised states of 2-TU. We optimised the geometry of the lowest valence singlet ( $S_0$ ,  $S_1$ ,  $S_2$ ) and triplet ( $T_1$ ,  $T_2$ ,  $T_3$ ) states with and without the constraint of planarity. Since the  $S_0$  minimum is nearly planar, the excited state (unstable) planar minima are likely to play a role in the short time dynamics and are marked with an asterisk in Figs. 3 and 4. Fully-optimised, stable non-planar minima could be found for the  $S_1$ ,  $S_2$  and  $T_1$  states. The computational details are given in the Methods section and more extended in Supplementary Discussion 3.

For each optimised geometry and each valence state we calculated the binding energy of the electrons in the three 2p core orbitals of the S atom. We estimated the ionization cross sections as proportional to the norm of the associated Dyson orbitals and used these data to simulate pump-probe photoelectron spectra at different geometries. The stick spectrum (shown in the Supplementary Discussion 4) was convoluted with a Gaussian of a FWHM of 3.5 eV, to match the width of the experimental bands.

## Discussion

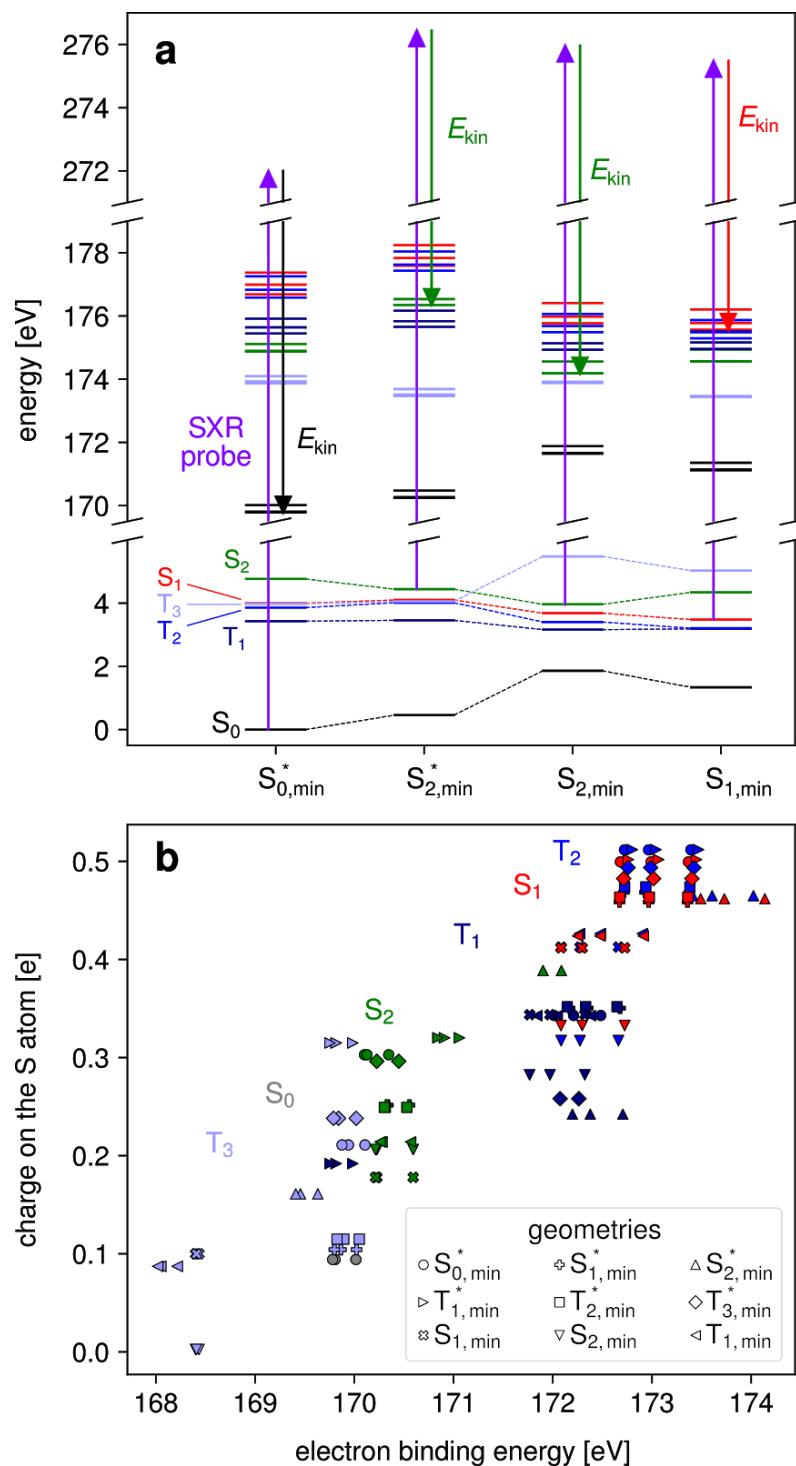


Figure 3: Soft X-ray photoelectron probing of the excited-state dynamics of 2-thiouracil. (a) Calculated electronic energies for the valence excited states, in the range 0-6 eV, and the core ionised states, in the range of 170-179 eV, for four geometries relevant in the short time

dynamics. The arrows illustrate the  $2p^{-1}$  ionisation process associated with the most intense transition. The core ionised states are grouped into sets of three states, which follow the color coding of the valence states, meaning that their valence configuration is maintained with a  $p_x$ ,  $p_y$  or  $p_z$  core hole. Accordingly, the electron kinetic energy  $E_{kin}$  refers to ionisations out of  $S_0$ ,  $S_1$  and  $S_2$ , depending on the geometry. (b). Partial charges on the S atom plotted against the binding energy of the 2p electrons, calculated for the valence states at nine different geometries. For each geometry, the graph includes three markers for each excited state ( $S_1$ ,  $S_2$ ,  $T_1$ ,  $T_2$ ,  $T_3$ ); in addition, three dots are included for the ionisation from  $S_0$  at  $S_{0,min}^*$ , for a total of  $9 \times 3 \times 5 + 3 = 138$  markers. Asterisks denote restriction in the calculation of the states to planar geometries.

The difference spectra, with their shift to lower kinetic energies, indicate an increased IP of the UV excited states. This is correctly predicted by the *ab initio* calculations, as illustrated by Fig. 3a, which shows the energies of the valence-excited and core-ionised states computed for different molecular geometries. The core-ionised states are reached by ionization of 2p electrons and are colour-coded according to the precursor valence states. For 2-thiouracil in the  $S_1$  and  $S_2$  states, the kinetic energy of the ejected electron is lower than for the ionization from  $S_0$ .

The classical static XPS connects the IP of a particular element on a particular site within a molecule to the total charge at the probed atom, which is related to the electronegativity of the nearest neighbor atoms<sup>29</sup>. Accordingly we speculate if this model can be applied in a dynamic context and that the long lasting shift of the kinetic energy indicates that the net effect of the photoexcitation is charge redistribution away from sulphur. To prove this statement, we performed a Löwdin-population-analysis on the wavefunctions of the different electronic states at the different geometries, which yields partial charges on the atoms of the molecule. In Fig. 3b the calculated partial charge on the S atom is plotted against the core electron binding energy. We identify a positive charge on the sulphur atom in the photoexcited states. Even more remarkable is the linear relation between binding energy and charge. This essentially reduces the IP, which is the difference in total electronic energy of core-ionised and neutral states to the local charge at the probed atom, within the uncertainty given by the scatter of points. This allows us to invert shifts in the kinetic energy to changes in the charge at the probe atom, which is an important molecular quantity in itself. Even more, local charge changes can be connected to electronic or nuclear dynamics either by chemical intuition or by exclusive calculations of the valence states without the need of computing core-ionised states.

In addition, we observe important trends that demonstrate the sensitivity of x-ray methods for time-resolved electronic spectroscopy. The colors in Fig. 3 indicate the electronic state while the different symbols indicate geometries, corresponding to minima or saddle points on different potential energy surfaces. We clearly observe clustering according to electronic state, although very widely differing geometries have been used. Thus the main factor for local charge and therefore binding energy is the electronic state of the molecule. This in turn gives core-level

photoelectron spectroscopy electronic state sensitivity. The exceptions of one  $S_2$  and  $T_1$  geometry are explained in the Supplementary discussion 5. The data for the  $S_1$  and  $T_2$  states are very well clustered in the upper right corner of Fig. 3b, with the highest IP. These states have  $n\pi^*$  character and possess a high positive charge on the sulphur atom, because of the highly-localised half-occupied  $n$  lone pair orbital, as illustrated in Fig. 1.

The onset of the experimental difference feature around time-zero is shown in more detail in the waterfall plot of Fig. 4a. The difference signal gets stronger with delay indicating an increasing  $f$  over the time-resolution of 191 fs. We initially identify the development of the negative feature sitting stable at 104 eV and a comparatively broader positive feature at lower kinetic energies.

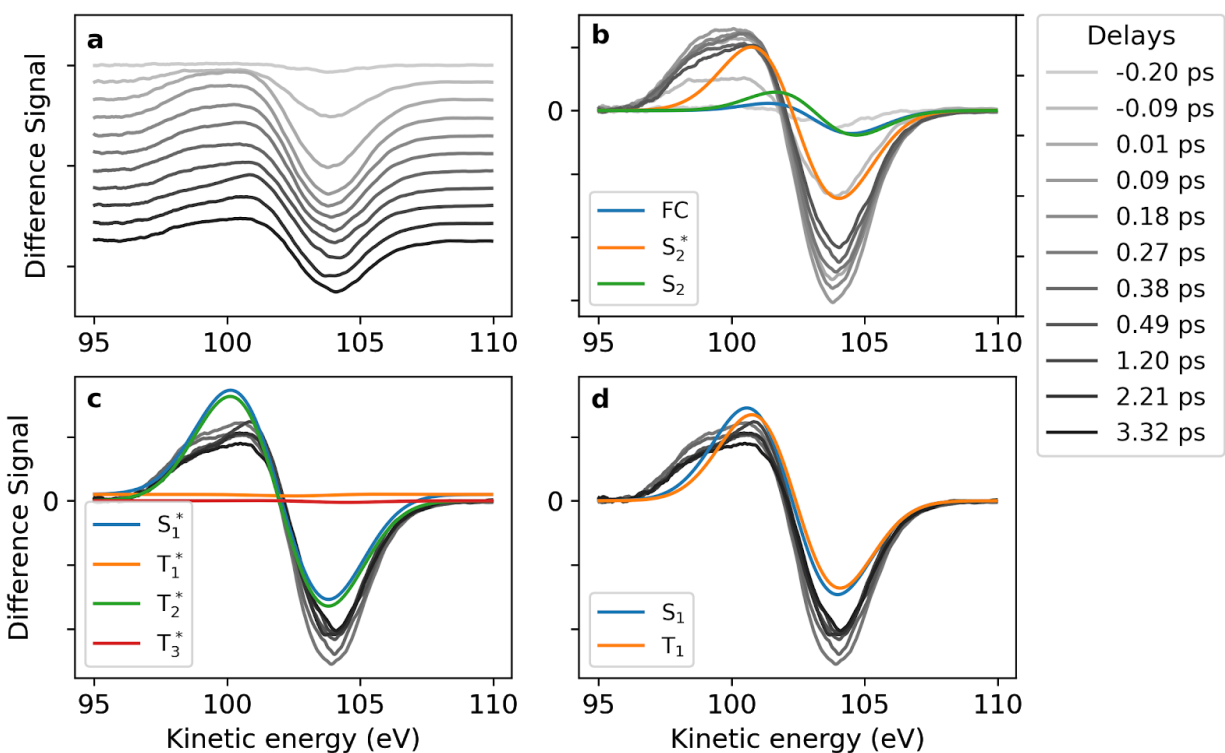


Figure 4: (a) Ridgeline plot of experimental difference spectra for different pump-probe delays between -0.2 to 3.3 ps. (b - d) Comparison of experiment with theoretical difference spectra computed at the coupled-cluster level of theory. All calculated difference spectra are shifted lower in kinetic energy by 1.3 eV. (b) shows spectra with delays in the range -0.2 to 0.49 ps, (c) and (d) spectra with delays 0.27 to 3.32 ps. The theoretical spectra use the energies at the minima of the respective geometry (e.g.  $S_2$  is  $S_2$  minimum at  $S_2$  geometry) except for FC which is the  $S_2$  minimum in ground state ( $S_0$ ) geometry. Asterisks denote restriction in the calculation of the states to planar geometries.

The 200 fs decay of the difference feature indicates relaxation of the molecular population either back into the ground state, into states with negligible photoionization cross section, or into states with an IP equal to the ground state. To obtain more insight, we compare the experimental XPS to simulations in Fig. 4b-d. Figure 4b shows the  $S_2$  state difference spectra and three different molecular geometries. Figure 4c shows spectra with 'unstable' planar geometries. The most important is the  $S_1$  state, others are expected to play a minor role in the dynamics for short times<sup>38,39</sup>. Figure 4d shows difference spectra for the  $S_1$  and  $T_1$  states at their respective potential energy minimum geometry. The unstable  $T_1^*$  and  $T_3^*$  spectra are indeed flat on our scale and could in principle explain the observed decay in difference amplitude. However, these geometries cannot be stable, and cannot explain the long-lasting reduction in amplitude with the 200 fs exponential decay. In addition, the remaining non-flat difference spectra do not exhibit a large enough difference. We therefore attribute the observed decay to an ultrafast relaxation into the electronic ground state with a 200 fs time-constant.

We compare early difference spectra to the calculated spectra of the directly photoexcited  $S_2$  state in different geometries in Fig. 4b. The best representation is given by the  $S_2^*$  planar geometry, which resembles the zero crossing best. The missing low-energy wing from 97-98.5 eV in the theoretical spectra can likely be attributed to the fact that we neglect wave-packet and incoherent thermal distribution effects resulting in extended geometry coverage. In addition, we do not model shake-up phenomena that would also contribute to a lower kinetic energy range. The Franck-Condon (FC) spectrum should be included in difference spectra, however, the short lifetime of this point as compared to our time-resolution makes it a minor contributor. We can however exclude a relaxation with major contributions from the  $S_2$  out-of-plane minimum (green line), as this would mean a shift in the zero-crossing feature by about 1 eV to higher kinetic energies, which is not observed in the experiment.

To analyze the picosecond difference spectra, we compare them to calculated difference spectra in Fig. 4c and d. The restricted planar minima/saddle points of  $S_1$  and  $T_2$  (Fig. 4c) could be responsible for parts of the difference spectra for a limited time until relaxation into a non-planar geometry. Among these non-planar geometries, both the  $S_1$  and  $T_1$  show agreement with the experimental difference spectrum, although again the low-energy tail in the experimental difference spectrum is not reproduced. While those states cannot be distinguished within our spectral resolution, we remark that simulations/experiments on the pyrimidine nucleobases call for the  $S_1$   $^1n\pi^*$  state to be occupied first after  $S_2$  relaxation<sup>43</sup>. Only thereafter will the triplet states gain population. Based on the experimental features, we can exclude the planar geometries of the  $T_1$  and  $T_3$  states to play a major role in the relaxation process.

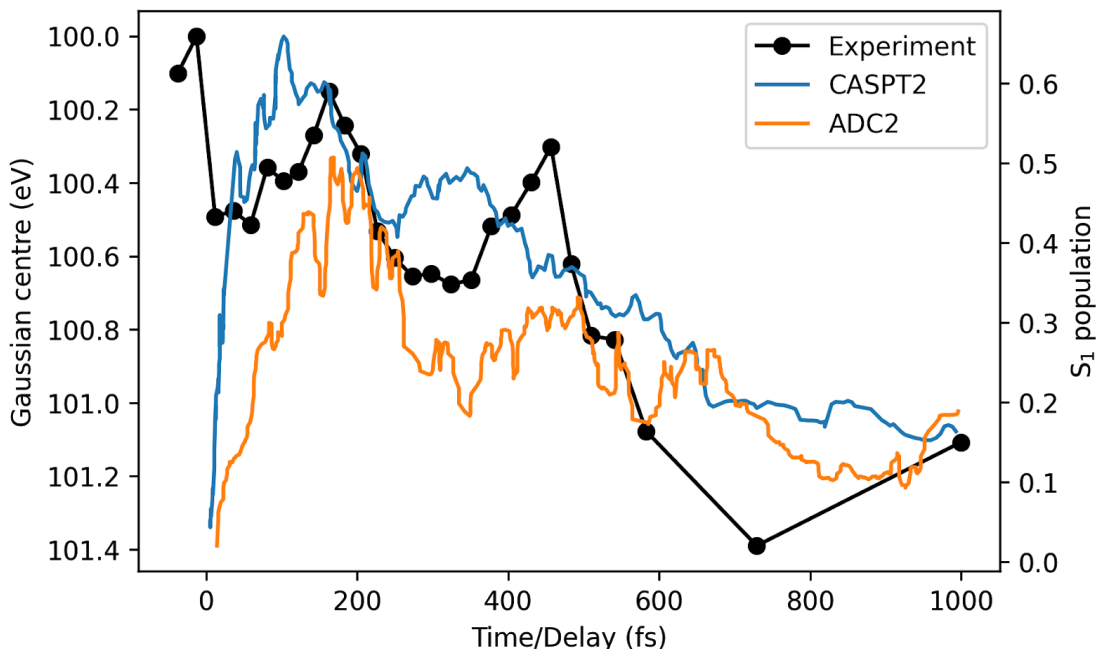


Figure 5: Comparison of the oscillation dynamics in the spectral position with trajectory simulations. The fitted Gaussian centre (black dots, left scale) for the positive lobe from Fig. 2 is compared with the population of the  $S_1$  state, derived from CASPT2 calculations from Ref. <sup>38</sup> (blue line) and ADC(2) calculations from Ref. <sup>39</sup> (orange line, both on the right scale). The experimental 250 fs oscillation features have their counterparts in the simulated  $S_1$  population, indicating the observation of a population exchange between the  $S_1$  state and other electronic states.

We now turn to the 250 fs oscillations in the spectral centre of the positive lobe in Fig. 2c. A normal mode analysis at various minima did yield a 250 fs oscillation only at the  $S_2$  nonplanar minimum. However, we believe that this is not the origin of the spectral modulation as we have shown above that the  $S_2$  nonplanar minimum can be neglected in the relaxation process. Instead, the  $S_1$  and triplet states are major contributors on the picosecond timescale. In order to gain further insight on the physical origin of the oscillation, we plot our spectral centre together with the  $S_1$  state population from the trajectory surface-hopping calculations of Mai et al. <sup>38,39</sup> in Fig. 5. The  $S_1$  populations calculated using an CASPT2 and ADC(2) approach show an oscillation with around 250 fs period, which is more pronounced in the case of ADC(2). The simulations predict a transfer of population among the  $S_1$ ,  $S_2$  and triplet states in a coherent fashion and the details of states participating in the population dynamics depends on the applied electronic structure method. However, in both cases, the  $S_1$  state, having the highest IP of all states, carries the largest oscillation. From this comparison we deduce that we observe the coherent exchange of population among different electronic states. The change in spectral position is induced by the fact that different states involved in this dynamics have slightly different IPs, which is picked up by the fitted spectral center.

In summary, we confirm part of the proposed relaxation pathway for the molecule and suggest a new, previously not observed, relaxation channel. From the comparison of delay-dependent difference spectra with simulated difference spectra, we deduce that the molecular population is not found to a large extent in the out-of-plane minimum of the  $S_2$  state. This agrees with the predictions of trajectory calculations when using a CASPT2 approach to electronic structure<sup>38</sup> but is in contrast to trajectory calculations with a ADC(2) electronic structure approach<sup>39</sup>. While in the first reference the  $S_2$  lifetime is below 100 fs and thus too short for the molecule to effectively reach out of plane geometries, the latter predicts an  $S_2$  lifetime of 250 fs which allows for out of plane geometries. We furthermore confirm the  $S_1$  and  $T_1$  states as major paths in the relaxation, in agreement with past experimental/theoretical studies<sup>35,36</sup>.

Ground state relaxation has been observed before in the solution as well as in the gas phase<sup>34,44</sup> with time constants of 50 to 200 ps in the gas phase, attributed to triplet-to-ground state relaxation<sup>34</sup>. Here we propose an additional and ultrafast ground state decay channel of 200 fs lifetime. The channel is close to the measured time constant around 300 fs, that has been attributed to intersystem crossing in Ref.<sup>34</sup>.

Finally, we observe coherent population exchange between different electronic states in the positive spectral center of the difference spectra. A comparison with the  $S_1$  population in trajectory-based simulations<sup>38,39</sup> in Fig. 5 shows an agreement in the beating period. On further inspection, the period predicted by the ADC(2) method fits our observed period better, however the calculations used different excitation energies which could alter this oscillation.

## Conclusion

We investigated the ultrafast molecular relaxation of UV excited 2-thiouracil using TR-XPS at the sulphur 2p edge. We show that electronic state relaxation is reflected in the difference photoelectron spectra and that our measured spectra are in agreement with a sub-100 fs relaxation from the  $S_2$  state into lower lying  $S_1$  and  $T_1$  states. In contrast to all other measurements we find an ultrafast 200 fs relaxation of  $\frac{1}{3}$  of the photoexcited population back to the electronic ground state. The data show a 250 fs spectral oscillation in the positive feature of the difference spectrum. We interpret this as an oscillation in the electronic state population in agreement with past trajectory simulations.

We find that the main change in kinetic energy is due to different electronic states. However the molecular geometry has some, although smaller, effect on the kinetic energy shift. More generally, we establish that the shift in the electron kinetic energy is linearly dependent on the local charge of the atom to be probed by TR-XPS. In future, one can address more than one site of the molecule using TR-XPS. This facilitates the determination of local charge change maps upon photoexcitation.

## Methods

**Time-resolved UV pump soft x-ray probe (photo-) electron spectroscopy:** The experiment was performed at the FL24 beamline of the FLASH2 facility at DESY using the newly built URSA-PQ apparatus. A detailed description of the apparatus and the experiment can be found elsewhere<sup>45,46</sup>. In short, the apparatus includes a magnetic bottle time-of-flight electron

spectrometer (MBES), a capillary oven to evaporate the 2-thiouracil samples at 150°C and a paddle with beam diagnostics on top of the oven. UV pump pulses of 269 nm center wavelength, 80 fs duration and an energy below 1  $\mu$ J were focused to a 50  $\mu$ m focus to pre-excite the molecules into the  $\pi\pi^*$  state. Power scans on the time-dependent spectral features were performed to assure that the signal is not over-pumped by the UV pulses (Supplementary Discussion 6).

The tunable soft x-ray pump pulses were produced via SASE (self-amplified spontaneous emission) radiation. Every second x-ray pulse was delivered without UV excitation for obtaining a reference on the non-excited molecule. The mean x-ray photon energy was set to 272 eV with a bandwidth of 1-2 % (including jitter). The x-ray probe was linearly polarised parallel to the axis of the magnetic bottle spectrometer and the UV polarization. The focal size of the x-ray beam was slightly larger than the UV spot. Systematic power scans were performed to exclude nonlinear effects in the x-ray induced electron spectra (see SI). To increase energy resolution of the spectrometer, the speed of the ejected electrons was reduced by an -80 V retardation voltage on an electrostatic lens in front of the 1.7 m long flight tube which was kept at a constant potential. The energy resolving power of the MBES ( $E/\Delta E$ ) has been determined with Kr MNN Auger lines to be 40 at 0 V retardation. Based on the sulphur 2p photoline, we estimate the resolution to be better than 30 with respect to the total kinetic energy. The time-dependent spectra were measured for a series of delays. In each scan, the delays were sorted randomly to avoid systematic effects. We measure the difference spectra by UV exciting the molecule for every second shot of the FEL pulse pattern. The data evaluation is described in Supplementary Discussion 7.

**Theoretical calculations:** The geometry optimization of ground state 2-thiouracil was performed using coupled-cluster theory with singles and doubles (CCSD) with the 6-311++G\*\* basis set<sup>47,48</sup>. Valence excited state optimizations and energy calculations at specific geometries were performed using the equation-of-motion formalism (EOM-CCSD) with the same basis set. All calculations were performed using the package Q-Chem 4.4<sup>49</sup>. At all computed geometries the valence excited states' wavefunctions are dominated by a singly-excited configuration. For the states  $S_1$ ,  $T_2$  ( $n\pi^*$ ) and  $S_2$ ,  $T_1$  ( $\pi\pi^*$ ) the involved orbitals at the Franck-Condon point are shown in Fig. 1. The structural parameters of the optimised planar and non-planar geometries on the different electronic states are reported in the Supplementary Information 3.

The binding energy of the electrons in the 2p orbitals of the sulphur atom were calculated using the equation-of-motion coupled-cluster method for IPs (EOM-IP-CCSD)<sup>50</sup> with the 6-311++G\*\* basis set for the S atom and the 6-31++G basis for all other atoms. Photoelectron intensities were approximated as the geometric mean of the norms of the left and right Dyson orbitals associated with the ionization process<sup>28</sup>. The target core-excited states of the cation were identified as the eigenstates which have the largest overlap with initial guess states, obtained by applying the annihilation operator of the three 2p electrons on reference CCSD wavefunctions, according to the procedure implemented in Q-Chem. To this end, reference CCSD wavefunctions for the different electronic states of the neutral molecule were calculated starting from unrestricted Hartree-Fock wavefunctions, which were optimised using the maximum overlap method (MOM), in order to mimic the (singly excited) orbital occupancy of the excited

states. A similar strategy to model the pump-probe ionization at the coupled-cluster level has been recently used by Vidal, Krylov and Coriani<sup>28</sup>. Spin-orbit coupling, leading to a splitting of the core-ionised states of the order of 1 eV (not resolved due to spectral broadening) is not included in the calculations.

## Acknowledgements

We thank the Volkswagen foundation for funding via a Lichtenberg Professorship.

We thank the BMBF for funding the URSA-PQ apparatus and for funding JM via Verbundforschungsproject 05K16IP1. We acknowledge DFG funding via Grants GU 1478/1-1 (MG) and SA547/17-1 (PS). TJAW was supported by the US Department of Energy, Office of Science, Basic Energy Sciences, Chemical Sciences, Geosciences, and Biosciences Division. RF thanks the Swedish Research Council (VR) and the Knut and Alice Wallenberg Foundation, Sweden, for financial support. We acknowledge DESY (Hamburg, Germany), a member of the Helmholtz Association HGF, for the provision of experimental facilities. Part of this research was carried out at FLASH2. FC acknowledges support from the European Research Council under the ERC-2014-StG STARLIGHT (Grant Agreement No. 637756).

## References

1. Domcke, W., Yarkony, D. R. & Köppel, H. *Conical intersections electronic structure, dynamics and spectroscopy*. (World Scientific Publishing Company, 2011).
2. Stolow, A., Bragg, A. E. & Neumark, D. M. Femtosecond Time-Resolved Photoelectron Spectroscopy. *Chem. Rev.* **104**, 1719–1758 (2004).
3. Rosspeintner, A., Lang, B. & Vauthey, E. Ultrafast Photochemistry in Liquids. *Annu. Rev. Phys. Chem.* **64**, 247–271 (2013).
4. Minitti, M. P. *et al.* Imaging Molecular Motion: Femtosecond X-Ray Scattering of an Electrocyclic Chemical Reaction. *Phys. Rev. Lett.* **114**, 255501 (2015).
5. Yang, J. *et al.* Diffractive Imaging of Coherent Nuclear Motion in Isolated Molecules. *Phys. Rev. Lett.* **117**, 173002 (2016).
6. Ischenko, A. A., Weber, P. M. & Miller, R. J. D. Capturing Chemistry in Action with Electrons: Realization of Atomically Resolved Reaction Dynamics. *Chem. Rev.* **117**, 11066–11124 (2017).
7. Kowalewski, M., Bennett, K. & Mukamel, S. Monitoring nonadiabatic avoided crossing dynamics in molecules by ultrafast X-ray diffraction. *Struct. Dyn.* **4**, 054101 (2017).
8. Yang, J. *et al.* Imaging CF<sub>3</sub>I conical intersection and photodissociation dynamics with ultrafast electron diffraction. *Science* **361**, 64–67 (2018).
9. Wolf, T. J. A. *et al.* The photochemical ring-opening of 1,3-cyclohexadiene imaged by ultrafast electron diffraction. *Nature Chem.* **11**, 504–509 (2019).
10. Bergmann, U., Yachandra, V. & Yano, J. *X-Ray Free Electron Lasers: Applications in Materials, Chemistry and Biology*. (Royal Society of Chemistry, 2017).
11. Young, L. *et al.* Roadmap of ultrafast x-ray atomic and molecular physics. *J. Phys. B: At. Mol. Opt. Phys.* **51**, 032003 (2018).

12. Bressler, C. & Chergui, M. Ultrafast X-ray Absorption Spectroscopy. *Chem. Rev.* **104**, 1781–1812 (2004).
13. Zhang, W. *et al.* Tracking excited-state charge and spin dynamics in iron coordination complexes. *Nature* **509**, 345–348 (2014).
14. Neville, S. P. *et al.* Beyond structure: ultrafast X-ray absorption spectroscopy as a probe of non-adiabatic wavepacket dynamics. *Faraday Discuss.* **194**, 117–145 (2016).
15. Neville, S. P. *et al.* Excited state X-ray absorption spectroscopy: Probing both electronic and structural dynamics. *J. Chem. Phys.* **145**, 144307 (2016).
16. Segatta, F. *et al.* Exploring the capabilities of optical pump X-ray probe NEXAFS spectroscopy to track photo-induced dynamics mediated by conical intersections. *Faraday Discuss.* **221**, 245–264 (2020).
17. Attar, A. R. *et al.* Femtosecond x-ray spectroscopy of an electrocyclic ring-opening reaction. *Science* **356**, 54–59 (2017).
18. Pertot, Y. *et al.* Time-resolved x-ray absorption spectroscopy with a water window high-harmonic source. *Science* **355**, 264–267 (2017).
19. Bhattacharjee, A., Pemmaraju, C. D., Schnorr, K., Attar, A. R. & Leone, S. R. Ultrafast Intersystem Crossing in Acetylacetone via Femtosecond X-ray Transient Absorption at the Carbon K-Edge. *J. Am. Chem. Soc.* **139**, 16576–16583 (2017).
20. Loh, Z.-H. *et al.* Observation of the fastest chemical processes in the radiolysis of water. *Science* **367**, 179–182 (2020).
21. Wolf, T. J. A. *et al.* Probing ultrafast  $\pi\pi^*/n\pi^*$  internal conversion in organic chromophores via K-edge resonant absorption. *Nature Comm.* **8**, 29 (2017).
22. Ehlert, C., Gühr, M. & Saalfrank, P. An efficient first principles method for molecular pump-probe NEXAFS spectra: Application to thymine and azobenzene. *J. Chem. Phys.* **149**, 144112 (2018).
23. Brauße, F. *et al.* Time-resolved inner-shell photoelectron spectroscopy: From a bound molecule to an isolated atom. *Phys. Rev. A* **97**, 043429 (2018).
24. Leitner, T. *et al.* Time-resolved electron spectroscopy for chemical analysis of photodissociation: Photoelectron spectra of  $\text{Fe}(\text{CO})_5$ ,  $\text{Fe}(\text{CO})_4$ , and  $\text{Fe}(\text{CO})_3$ . *J. Chem. Phys.* **149**, 044307 (2018).
25. Bennett, K., Kowalewski, M. & Mukamel, S. Nonadiabatic Dynamics May Be Probed through Electronic Coherence in Time-Resolved Photoelectron Spectroscopy. *J. Chem. Theory Comput.* **12**, 740–752 (2016).
26. Neville, S. P., Chergui, M., Stolow, A. & Schuurman, M. S. Ultrafast X-Ray Spectroscopy of Conical Intersections. *Phys. Rev. Lett.* **120**, 243001 (2018).
27. Inhester, L., Li, Z., Zhu, X., Medvedev, N. & Wolf, T. J. A. Spectroscopic Signature of Chemical Bond Dissociation Revealed by Calculated Core-Electron Spectra. *J. Phys. Chem. Lett.* **10**, 6536–6544 (2019).
28. Vidal, M. L., Krylov, A. I. & Coriani, S. Dyson orbitals within the fc-CVS-EOM-CCSD framework: theory and application to X-ray photoelectron spectroscopy of ground and excited states. *Phys. Chem. Chem. Phys.* **22**, 2693–2703 (2020).
29. Siegbahn, K. *ESCA applied to free molecules*. (North-Holland Pub. Co, 1969).
30. Arslançan, S., Martínez-Fernández, L. & Corral, I. Photophysics and Photochemistry of Canonical Nucleobases' Thioanalogs: From Quantum Mechanical Studies to Time Resolved

- Experiments. *Molecules* **22**, 998 (2017).
31. Zhang, X. *et al.* Novel DNA lesions generated by the interaction between therapeutic thiopurines and UVA light. *DNA Repair* **6**, 344–354 (2007).
  32. Brem, R., Daehn, I. & Karran, P. Efficient DNA interstrand crosslinking by 6-thioguanine and UVA radiation. *DNA Repair* **10**, 869–876 (2011).
  33. Ashwood, B., Pollum, M. & Crespo-Hernández, C. E. Photochemical and Photodynamical Properties of Sulfur-Substituted Nucleic Acid Bases. *Photochem. Photobiol.* **95**, 33–58 (2019).
  34. Sánchez-Rodríguez, J. A. *et al.* 2-Thiouracil intersystem crossing photodynamics studied by wavelength-dependent photoelectron and transient absorption spectroscopies. *Phys. Chem. Chem. Phys.* **19**, 19756–19766 (2017).
  35. Mohamadzade, A., Bai, S., Barbatti, M. & Ullrich, S. Intersystem crossing dynamics in singly substituted thiouracil studied by time-resolved photoelectron spectroscopy: Micro-environmental effects due to sulfur position. *Chem. Phys.* **515**, 572–579 (2018).
  36. Mai, S., Mohamadzade, A., Marquetand, P., González, L. & Ullrich, S. Simulated and Experimental Time-Resolved Photoelectron Spectra of the Intersystem Crossing Dynamics in 2-Thiouracil. *Molecules* **23**, 2836 (2018).
  37. Mai, S., Marquetand, P. & González, L. A Static Picture of the Relaxation and Intersystem Crossing Mechanisms of Photoexcited 2-Thiouracil. *J. Phys. Chem. A* **119**, 9524–9533 (2015).
  38. Mai, S., Marquetand, P. & González, L. Intersystem Crossing Pathways in the Noncanonical Nucleobase 2-Thiouracil: A Time-Dependent Picture. *J. Phys. Chem. Lett.* **7**, 1978–1983 (2016).
  39. Mai, S. *et al.* Surface hopping dynamics including intersystem crossing using the algebraic diagrammatic construction method. *J. Chem. Phys.* **147**, 184109 (2017).
  40. Giuliano, B. M. *et al.* Tautomerism in 4-Hydroxypyrimidine, S -Methyl-2-thiouracil, and 2-Thiouracil. *J. Phys. Chem. A* **114**, 12725–12730 (2010).
  41. Plekan, O. *et al.* Functionalisation and immobilisation of an Au(110) surface via uracil and 2-thiouracil anchored layer. *Phys. Chem. Chem. Phys.* **17**, 15181–15192 (2015).
  42. Föhlisch, A. *et al.* Direct observation of electron dynamics in the attosecond domain. *Nature* **436**, 373–376 (2005).
  43. Improta, R., Santoro, F. & Blancafort, L. Quantum Mechanical Studies on the Photophysics and the Photochemistry of Nucleic Acids and Nucleobases. *Chem. Rev.* **116**, 3540–3593 (2016).
  44. Yu, H. *et al.* Internal conversion and intersystem crossing pathways in UV excited, isolated uracils and their implications in prebiotic chemistry. *Phys. Chem. Chem. Phys.* **18**, 20168–20176 (2016).
  45. Metje, J. *et al.* URSA-PQ: A Mobile and Flexible Pump-Probe Instrument for Gas Phase Samples at the FLASH Free Electron Laser. *Applied Sciences* **10**, 7882 (2020).
  46. Lever, F. *et al.* Ultrafast dynamics of 2-thiouracil investigated by time-resolved Auger spectroscopy. *J. Phys. B: At. Mol. Opt. Phys.* **54**, 014002 (2020).
  47. Shavitt, I. & Bartlett, R. J. *Many – Body Methods in Chemistry and Physics: MBPT and Coupled-Cluster Theory*. (Cambridge University Press, 2009).
  48. Bartlett, R. J. & Musiał, M. Coupled-cluster theory in quantum chemistry. *Rev. Mod. Phys.*

- 79**, 291–352 (2007).
49. Shao, Y. *et al.* Advances in molecular quantum chemistry contained in the Q-Chem 4 program package. *Mol. Phys.* **113**, 184–215 (2015).
  50. Krylov, A. I. Equation-of-Motion Coupled-Cluster Methods for Open-Shell and Electronically Excited Species: The Hitchhiker’s Guide to Fock Space. *Annu. Rev. Phys. Chem.* **59**, 433–462 (2008).

## Supplemental information

### 1 Fits of the delay-dependent signals

The integral of the difference signal and the amplitudes from the double Gaussian fit show similar delay-dependent behaviour and have thus been fitted with the same function:

$$S(t) = \sum_{i=1}^2 A_i \cdot \exp\{-\tau_i^{-1} \cdot (t - t_0)\} \exp\{0.5 \cdot \tau_i^{-2} \cdot \sigma^2\} \left[ 1 + \operatorname{erf}\left(\frac{t - t_0 - \tau_i^{-1} \cdot \sigma^2}{\sqrt{2}\sigma}\right) \right] \quad (1)$$

The equation represents a Gaussian time-uncertainty function convoluted with two exponential decays. Here,  $A_i$  and  $\tau_i$  are the amplitude and decay constant of the  $i$ -th component.  $t_0$  is the time-zero, i.e. the overlap between pump and probe pulse, and  $\sigma$  describes the temporal resolution (with  $\sigma^2$  being the variance of the Gaussian function). The erf is the Gauss error function. The fitting range was restricted to -0.2 to +10 ps.

First, the integral of the absolute difference signal ( $S_{\text{int}}^{\text{abs}}$ ) was fitted. The fitted  $t_0$  value was used to correct the delays. Then, the integral of the positive ( $S_{\text{int}}^+$ ) and negative ( $S_{\text{int}}^-$ ) contributions to the difference spectra as well as the amplitudes from the Gaussian fits ( $S_{\text{amp}}^{+/-}$ ) were fitted with a fixed time uncertainty using the value from  $S_{\text{int}}^{\text{abs}}$ . The results of all five fits are summarised in table S1.

The full width at half maximum of the Gaussian time-uncertainty function is  $190 \pm 11$  fs. This value includes the pulse duration of the UV pump and the x-ray probe pulse as well as temporal jitter<sup>1,2</sup>. The time constant of the first decay component  $\tau_1$  lies between 200 and 300 fs for all fits with an average value of  $235 \pm 14$  fs. For the second decay constant  $\tau_2$ , only two fits give values within the picosecond range ( $\sim 200$  ps). The other values are within nano- or even microsecond range with similarly large fitting errors (noted with >1000 in table S1). Increasing the delay range for the fit does not improve the values for  $\tau_2$ . The values for  $\tau_1$  stay similar.

*Table S1: Fitted parameters of delay dependent amplitudes and integrals. \* after correcting the delays with value from  $S_{\text{int}}^{\text{abs}}$ . “-” indicates that value from  $S_{\text{int}}^{\text{abs}}$  has been used.*

	$S_{\text{int}}^{\text{abs}}$	$S_{\text{int}}^-$	$S_{\text{int}}^+$	$S_{\text{amp}}^-$	$S_{\text{amp}}^+$
$\sigma$ / fs	$81.1 \pm 4.5$	-	-	-	-
$t_0$ / fs	$-56.1 \pm 3.8$	$2.4 \pm 3.6^*$	$-6.2 \pm 6.4^*$	$1.5 \pm 2.9^*$	$4.7 \pm 3.5^*$
Amp 1	$43.4 \pm 3.9$	$31.1 \pm 1.5$	$12.4 \pm 1.5$	$10.39 \pm 0.91$	$4.02 \pm 0.41$
$\tau_1$ / fs	$225 \pm 27$	$247 \pm 22$	$221 \pm 38$	$211 \pm 38$	$290 \pm 62$
Amp 2	$46.5 \pm 1.5$	$28.15 \pm 0.80$	$17.45 \pm 0.60$	$11.32 \pm 0.41$	$5.21 \pm 0.22$
$\tau_2$ / ps	$200 \pm 140$	>1000	>1000	$140 \pm 140$	>1000
offset	$1.8 \pm 1.2$	$0.99 \pm 0.62$	$0.72 \pm 0.55$	$0.511 \pm 0.065$	$-0.066 \pm 0.051$

## 2 Magnetic bottle sensitivity

The data shown in the following plots (Fig. S1 to S3) were recorded on a follow up beamtime to investigate the influence of different experimental parameters on the photoelectron spectra.

In Fig. S1, the solenoid (coil) current and thus the magnetic field inside the flight tube was changed. The electron spectra were recorded with a photon energy of 272 eV at a delay of 200 ps and a retardation voltage of -80 V. Panel a) shows the normalised difference spectra of the sulphur 2p photoline. The positive (red) and negative (blue) contributions broaden with increasing magnetic field and also shift towards lower kinetic energy. Additionally, panel b) shows the integrals of the positive and negative contributions of the spectra. The two lobes change signal strength in a counter-oscillatory way. Especially the negative lobe is stronger than the positive one at 200 mA which was the value also used for the data presented in this paper.

In Fig. S2, the coil current was kept constant at 200 mA and instead the retardation voltage was scanned across -80 V, while the kinetic energy is corrected for the change in retardation potential. Again, panel a) shows the difference spectra and b) the integrals of the positive and negative contributions. The counter-oscillation of the two lobe integrals is again observed. This is also the case for a photon energy scan around 272 eV shown in Fig. S3 where the coil current and retardation voltage are kept constant at values of 200 mA and -80 V, respectively.

Our systematic investigations of the difference spectra for various experimental settings exhibit the influence of cyclotron resonances on the relative amplitudes in the MBES, an aspect which is well known for this kind of electron spectrometer<sup>3</sup>. In future runs, the characterisation might be used to calibrate the MBES sensitivity.

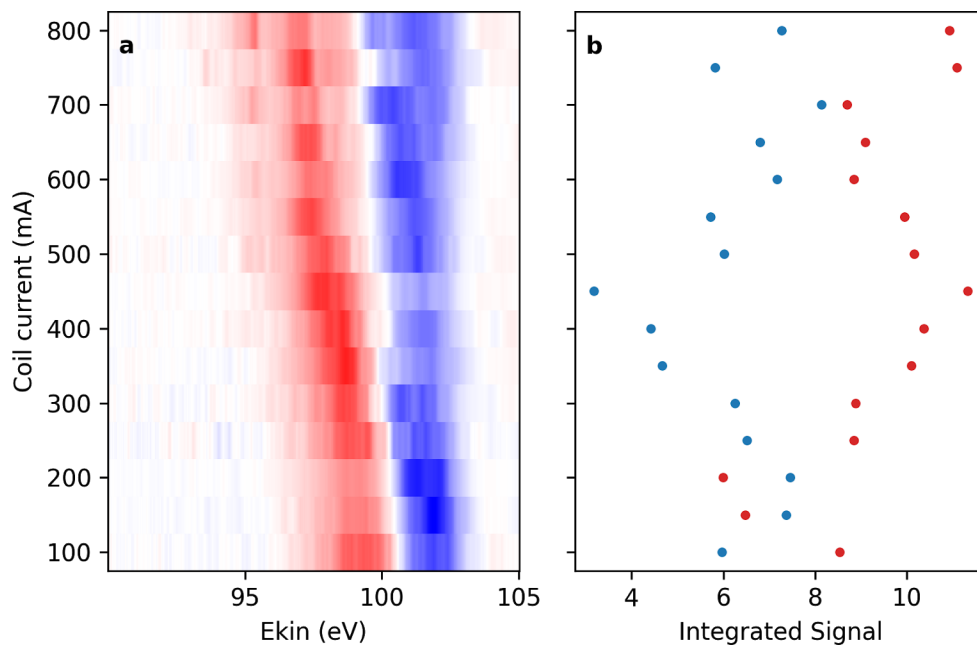


Figure S1: Scan of the coil current on the flight tube at 272 eV x-ray photon energy and -80 V retardation. a: false-color representation of the difference spectra of the photoline. b: integrated signal of positive (red) and negative (blue) contributions.

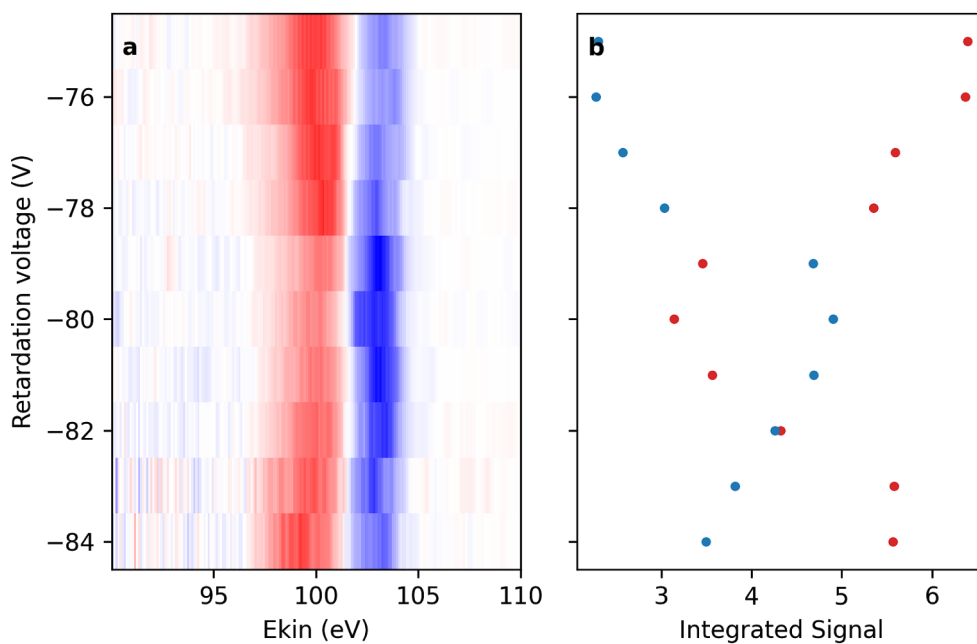


Figure S2: Scan of the retardation voltage at 272 eV and 200 mA coil current. a: false-color representation of the difference spectra of the photoline. b: integrated signal of positive (red) and negative (blue) contributions.

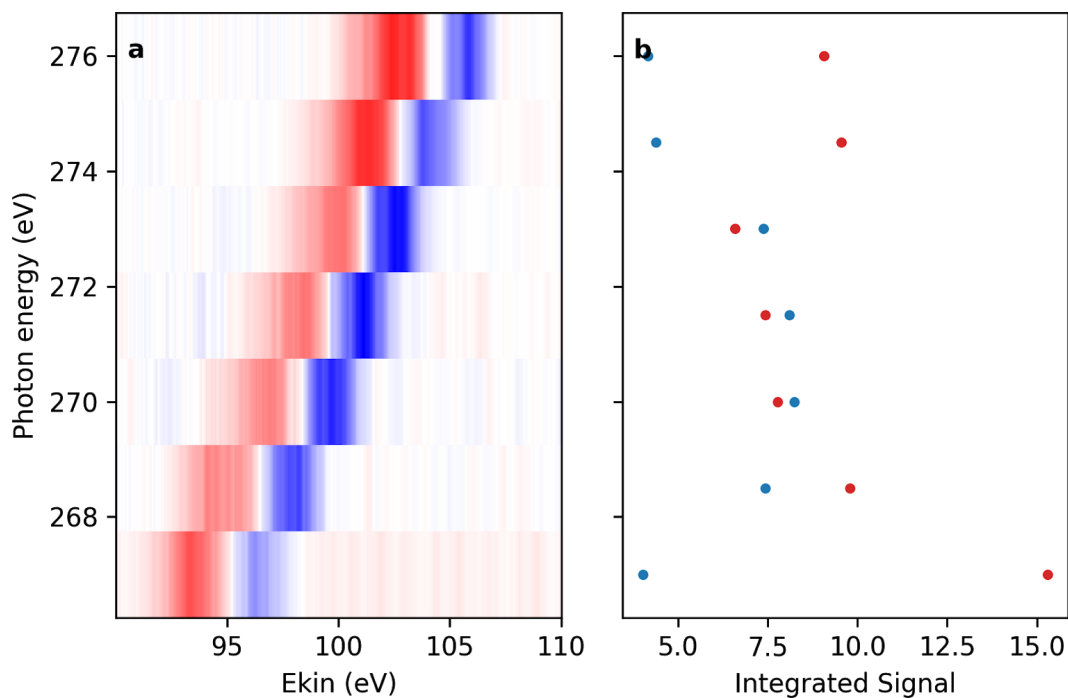


Figure S3: Scan of the photon energy at 80V retardation and 200mA coil current. a: false-color representation of the difference spectra of the photoline. b: integrated signal of positive (red) and negative (blue) contributions.

### 3 Quantum chemical results

The structure and the atom numbering of 2-thiouracil is shown in Fig. S4. The most relevant molecular orbitals involved in the valence excitations are depicted in Fig. S5 for the Franck-Condon geometry. The singlet states  $S_1$  and  $S_2$  have  $n\pi^*$  and  $\pi\pi^*$  character, respectively. At planar geometries, they originate from  $27a' \rightarrow 7a''$  and  $6a'' \rightarrow 7a''$  transitions. The triplet states  $T_1$  and  $T_2$  originate mainly from the same transitions of  $S_2$  and  $S_1$ , apart from the spin-flipping, and therefore they have  $\pi\pi^*$  and  $n\pi^*$  character, respectively.  $T_3$  has a  $\pi\pi^*$  character and is mostly contributed by the transitions  $5a'' \rightarrow 7a''$  and, to a lesser extent,  $6a'' \rightarrow 8a''$ .

Table S2 reports the main structural parameters of the optimized geometries. The planar equilibrium structures are indicated by an asterisk ( $S_{0,\min}^*$ ,  $S_{1,\min}^*$ , etc.); the non-planar geometry optimization of the states  $T_2$  and  $T_3$  did not converge to a stationary point. At all minima, except for  $T_{1,\min}^*$ , the C-S bond is elongated by  $\approx 0.1$  Å as compared to  $S_{0,\min}$ . A larger elongation of about 0.25 Å is found in the state  $S_2$ . In the ground state the difference between the planar and non-planar minima  $S_{0,\min}^*$  and  $S_{0,\min}$  is negligible. In contrast, the states  $S_1$ ,  $S_2$  and  $T_1$  have non-planar minima which are depicted in Fig. S6 and involve an out-of-plane distortion of the C-S bond, with pyramidalization angles in the range  $\approx 35^\circ$ – $50^\circ$ . The stabilization energy,

associated with this out-plane distortion, is 0.30 eV, 0.48 eV and 0.17 eV for  $S_1$ ,  $S_2$  and  $T_1$ , respectively.

The comparison between Table S2 and Table 2 of Ref. <sup>4</sup> shows that the present optimized geometries agree very well with those obtained using the multi-state CASPT2 method. The main notable difference is a somewhat higher value of the pyramidalization angle  $\rho_{10324}$ , around the N atom bridging the C=S and C=O groups.

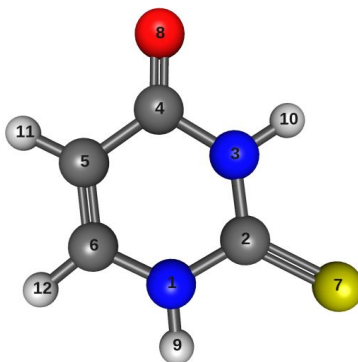


Figure S4: Structure and atom numbering of 2-thiouracil. The carbons are gray, the nitrogens are blue, the hydrogens are white, the oxygen is red and the sulphur is yellow.

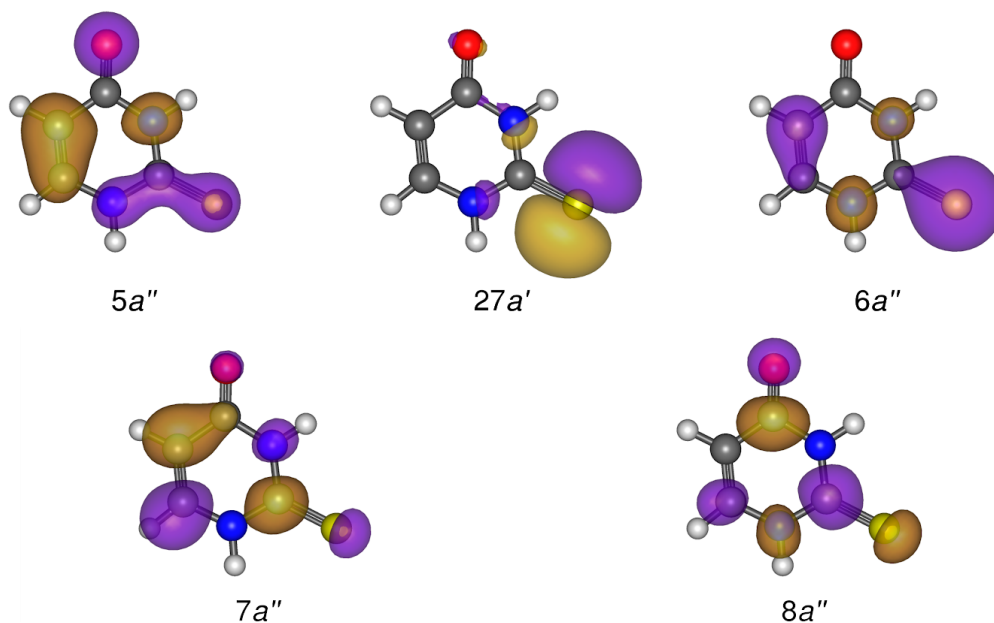


Figure S5: Most relevant orbitals involved in the valence excitations of 2-thiouracil, evaluated at the  $S_{0,min}^*$  geometry.

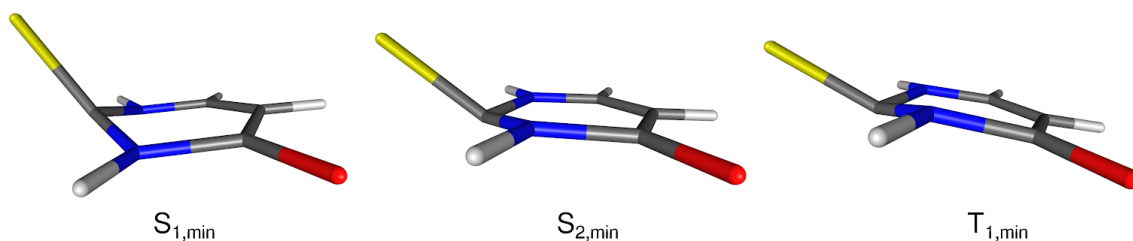


Figure S6: Optimized structures of the non-planar minima of the excited states of 2-thiouracil.

	planar geometries					
	$S_{0,\min}^*$	$S_{1,\min}^*$	$S_{2,\min}^*$	$T_{1,\min}^*$	$T_{2,\min}^*$	$T_{3,\min}^*$
energy [eV]	0.00	3.78	4.44	3.17	3.65	3.76
$r_{12}$	1.37	1.39	1.32	1.36	1.40	1.41
$r_{23}$	1.37	1.40	1.35	1.39	1.41	1.37
$r_{34}$	1.41	1.40	<b>1.47</b>	1.41	1.39	1.41
$r_{45}$	1.47	1.47	<b>1.42</b>	1.44	1.47	1.44
$r_{56}$	1.35	1.36	1.41	1.47	1.36	1.41
$r_{61}$	1.38	1.37	1.39	1.36	1.37	1.39
$r_{27}$	1.65	<b>1.74</b>	<b>1.76</b>	1.67	<b>1.73</b>	<b>1.70</b>
$r_{48}$	1.21	1.22	1.22	1.22	1.22	1.23
$\alpha_{127}$	122.8	122.1	120.5	121.7	122.2	121.3
$\alpha_{348}$	120.4	120.3	<b>116.0</b>	120.2	120.3	119.7
	non-planar geometries					
	$S_{0,\min}$	$S_{1,\min}$	$S_{2,\min}$	$T_{1,\min}$		
energy [eV]	0.00	3.48	3.96	3.00		
$r_{12}$	1.37	1.40	1.37	1.40		
$r_{23}$	1.37	1.40	1.38	1.41		

$r_{34}$	1.41	1.40	1.41	1.40
$r_{45}$	1.47	1.47	1.47	1.47
$r_{56}$	1.35	1.35	1.35	1.36
$r_{61}$	1.38	1.38	1.38	1.37
$r_{27}$	1.65	<b>1.77</b>	<b>1.90</b>	<b>1.77</b>
$r_{48}$	1.21	1.21	1.21	1.21
$\alpha_{127}$	122.8	<b>116.8</b>	<b>110.6</b>	<b>113.6</b>
$\alpha_{348}$	120.4	121.0	120.9	121.2
$\rho_{7213}$	-1.5	<b>34.0</b>	<b>48.8</b>	<b>42.5</b>
$\rho_{8435}$	-0.6	-3.2	0.8	2.1
$\rho_{10324}$	8.0	19.8	-10.8	-22.1
$\rho_{12651}$	1.5	-2.5	0.5	0.7

*Table S2: Geometrical parameters of the planar and non-planar equilibrium structures of the lowest electronic states of 2-thiouracil, optimized at the (EOM-)CCSD/6-311++G\*\* level. The largest structural changes with respect to  $S_{0,min}$  are highlighted in boldface. The bond distances  $r_{ij}$  are given in Å, the valence angles  $\alpha_{ijk}$  and the pyramidalization angles  $\rho_{ijkl}$  are in degrees.  $\rho_{ijkl}$  is defined as the angle between the vector of the  $i$ - $j$  bond and the  $kl$  plane. The dimension for the bond lengths is Å, for angles it is degrees.*

The EOM-CCSD electronic energies at the planar and non-planar minima of the different electronic states are reported in Table S3 and plotted in Fig. S7. The excitation energies at the ground state equilibrium ( $S_{0,min}$ ) are larger by  $\approx 0.4$  eV compared to those obtained by multi-reference calculations, although the spacing between the levels is similar. Indeed, the  $S_2 \leftarrow S_0$  vertical excitation energy agrees quite well with the experimental gas phase UV absorption spectrum of thiouracil<sup>5</sup>. As shown in Fig. S7, the potential energy surfaces of the states  $S_1$  and  $T_2$ , both of  $n\pi^*$  character are nearly parallel.

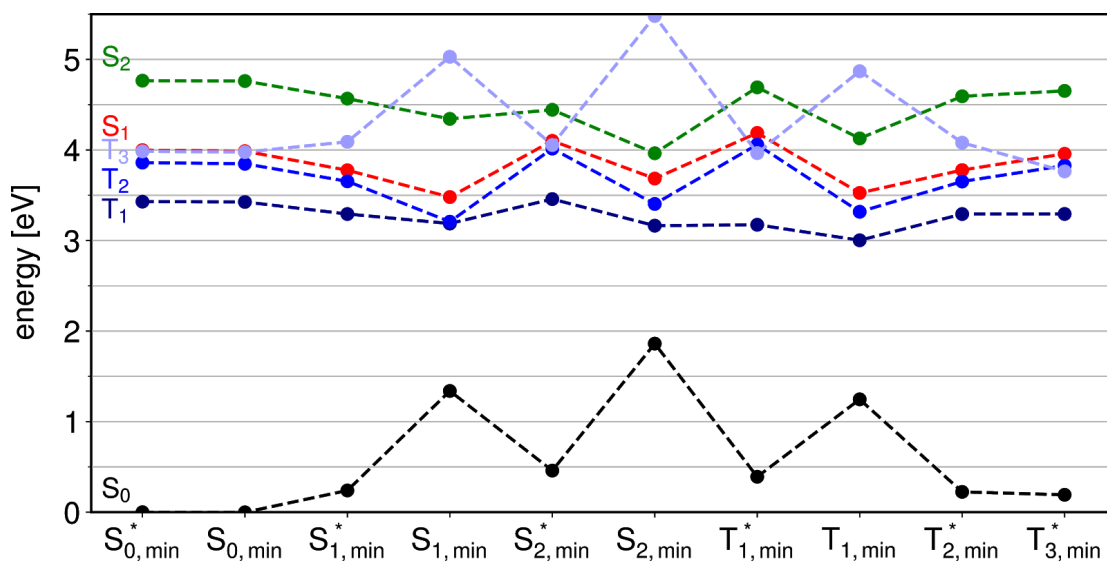


Figure S7: EOM-CCSD/6-311++G\*\* electronic energies of the lowest singlet and triplet states of 2-thiouracil, calculated at the planar and non-planar minima of the different states.

	State					
	S <sub>0</sub>	S <sub>1</sub>	S <sub>2</sub>	T <sub>1</sub>	T <sub>2</sub>	T <sub>3</sub>
	-	<sup>1</sup> (27a'→7a'')	<sup>1</sup> (6a''→7a'')	<sup>3</sup> (6a''→7a'')	<sup>3</sup> (27a'→7a'')	<sup>3</sup> (5a''→7a'') <sup>3</sup> (6a''→8a'')
S <sup>*</sup> <sub>0,min</sub>	0.00	4.00	4.77	3.43	3.86	3.98
S <sub>0,min</sub>	0.00	3.99	4.76	3.43	3.85	3.98
S <sup>*</sup> <sub>1,min</sub>	0.24	3.78	4.57	3.29	3.65	4.09
S <sub>1,min</sub>	1.34	3.48	4.34	3.19	3.21	5.03
S <sup>*</sup> <sub>2,min</sub>	0.46	4.10	4.44	3.46	4.02	4.05
S <sub>2,min</sub>	1.86	3.68	3.96	3.16	3.40	5.48
T <sup>*</sup> <sub>1,min</sub>	0.39	4.19	4.69	3.17	4.06	3.97
T <sub>1,min</sub>	1.25	3.53	4.13	3.00	3.32	4.87
T <sup>*</sup> <sub>2,min</sub>	0.22	3.78	4.59	3.29	3.65	4.08
T <sup>*</sup> <sub>3,min</sub>	0.19	3.96	4.65	3.29	3.82	3.76

*Table S3. EOM-CCSD/6-311++G\*\* electronic energies (in eV) of the lowest singlet and triplet states of 2-thiouracil, calculated at the planar and non-planar minima of the different states. For each state the dominant orbital transitions are reported. Energies are given in eV.*

#### 4 Calculated state- and geometry-dependent pump-probe XPS spectra

Photoelectron spectra are calculated at different geometries considering an ionisation process starting from the states S<sub>1</sub>, S<sub>2</sub>, T<sub>1</sub>, T<sub>2</sub> and T<sub>3</sub>. The reference “pump-off” spectrum, with ionisation starting from S<sub>0</sub>, is calculated only at the ground state minimum. For each geometry *x* the spectrum  $\sigma_n^x(E)$  from the state *n* is given as a sum of contributions associated with the three 2p orbitals,

$$\sigma_n^x(E) = C \sum_{i=1}^3 A_{in}^x g(E - E_{in}^x),$$

where *C* is a constant,  $E_{in}^x$  is the ionization potential from the 2p<sub>*i*</sub> orbital for the state *n* at the geometry *x*, evaluated by the EOM-IP-CCSD approach, and  $A_{in}^x$  is the ionization probability, approximated as the geometric average between the norms of the left and right Dyson orbitals<sup>6</sup>. The function *g*(·) is used to broaden the stick transitions in order to allow the comparison with experiment; the calculated profiles are obtained by applying a Gaussian broadening with a

standard deviation of 1.5 eV. Since in the EOM-IP-CCSD procedure the valence excited states are described by unrestricted wavefunctions, the two binding energies for the  $\alpha$  and  $\beta$  electrons differ by 0.0-0.1 eV and have been averaged in the calculation of  $E_{in}^x$ .

The (geometry-dependent) pump-probe signal  $S_n^x(E)$ , associated with population on a given state, is obtained as the difference

$$S_n^x(E) = \sigma_n^x(E) - \sigma_{S_0}^{S_{0,min}}(E) .$$

The calculated pump-probe spectra are shown in Figures S8 and S9 for the planar and non-planar geometries, respectively. Note the general trend for the binding energies  $T_3 < S_2 < T_1 < S_1 \approx T_2$ .

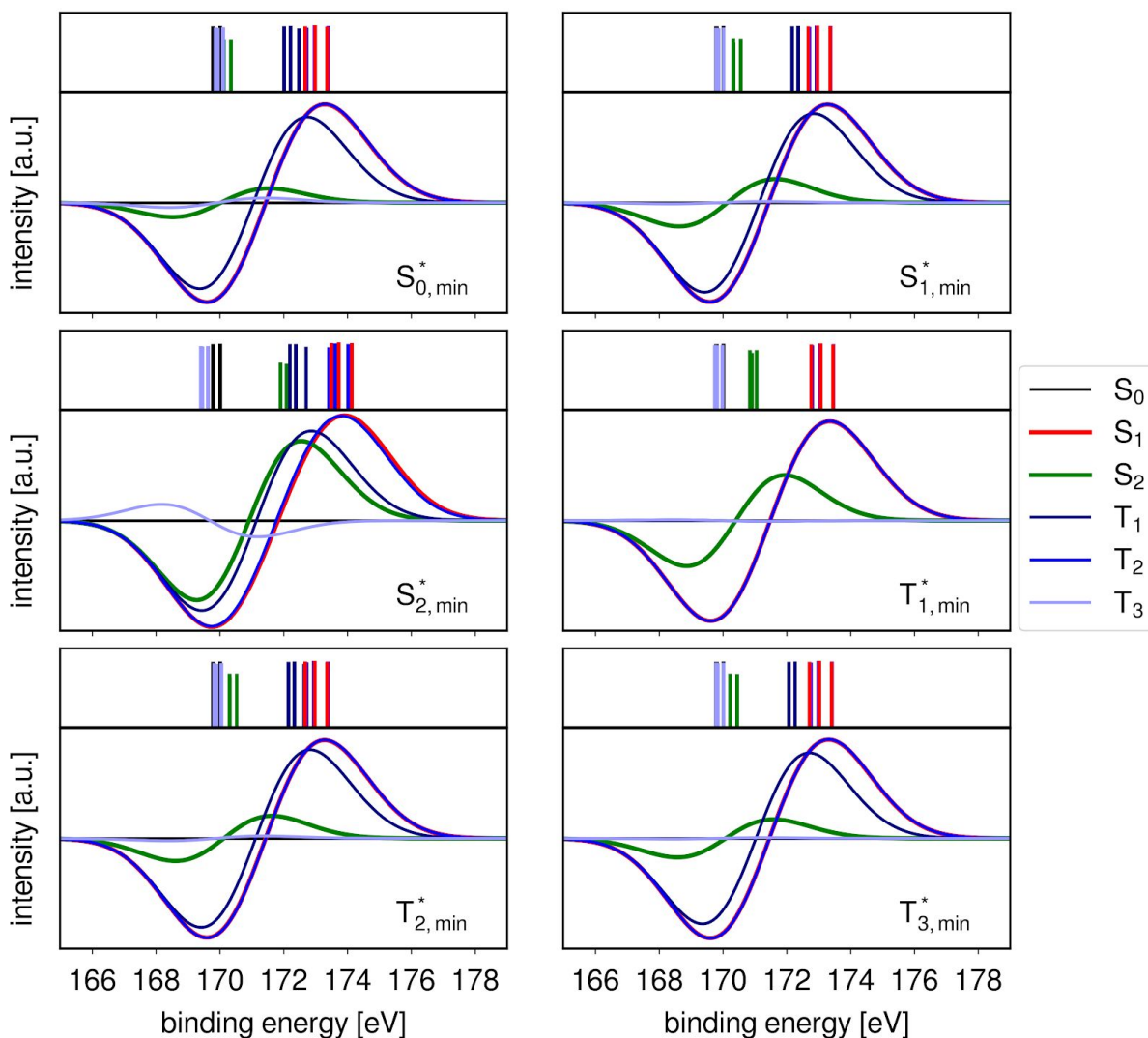


Figure S8. Binding energies of the 2p electrons (top panels) and pump-probe spectra (bottom panels) evaluated for different electronic states and different planar stationary geometries. The ionization intensities are estimated using Dyson orbital norms.

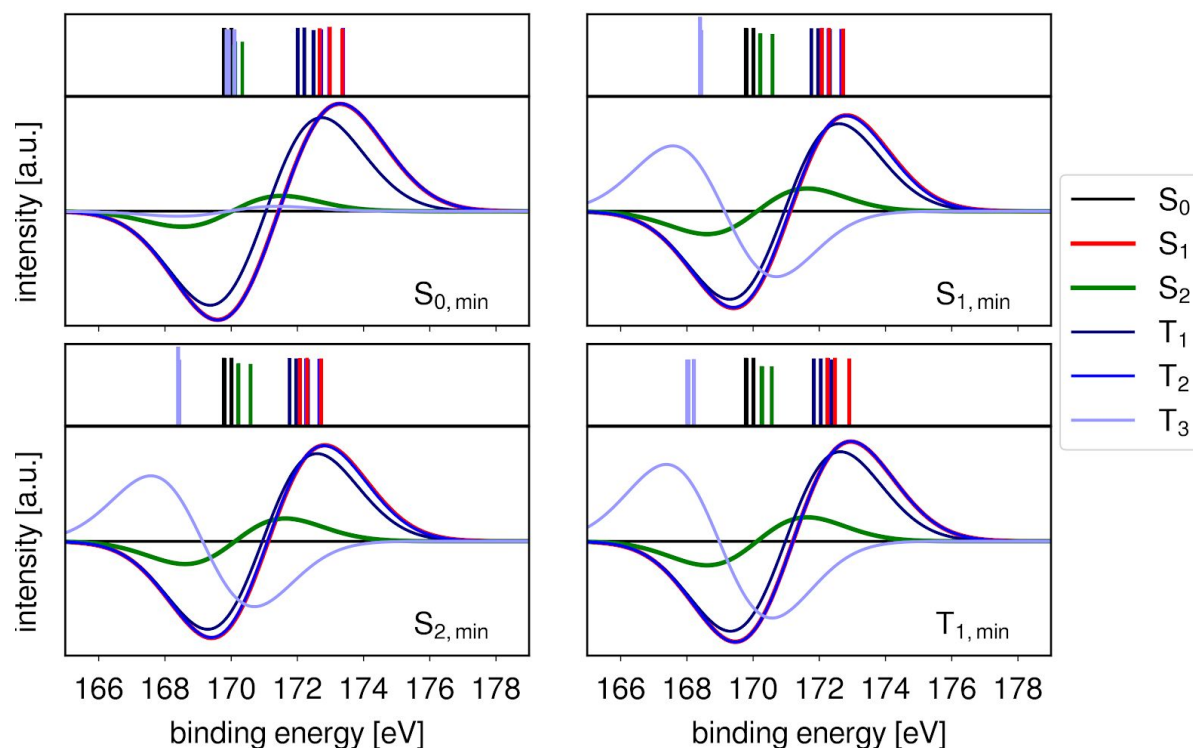


Figure S9. Binding energies of the 2p electrons (top panels) and pump-probe spectra (bottom panels) evaluated for different electronic states and different fully optimized geometries. The ionization intensities are estimated using Dyson orbital norms.

Soft X-ray photoelectron probing of the excited-state dynamics of 2-thiouracil. (a) Calculated electronic energies for the valence excited states, in the range 0-6 eV, and the core ionised states, in the range 170-179 eV, for four geometries relevant in the short time dynamics. The arrows illustrate the 2p-1 ionisation process associated with the most intense transition. The core ionised states are grouped into sets of three states, which follow the color coding of the valence states, meaning that their valence configuration is maintained with a  $p_x$ ,  $p_y$  or  $p_z$  core hole. Accordingly, the electron kinetic energy  $E_{kin}$  refers to ionisations out of  $S_0$ ,  $S_1$  and  $S_2$ , depending on the geometry. (b). Partial charges on the S atom plotted against the binding energy of the 2p electrons, calculated for the valence states at nine different geometries. For each geometry, the graph includes three dots for each excited state ( $S_1$ ,  $S_2$ ,  $T_1$ ,  $T_2$ ,  $T_3$ ); in addition, three dots are included for the ionisation from  $S_0$  at  $S_0^*,min$ , for a total of  $9 \times 3 \times 5 + 3 = 138$  dots.

### 5 Exceptions in the clustering according to electronic state

The data of Table S2 allow us to explain the exceptions in the clustering according to electronic states reported in Figure 3(b) of the main text. For example, the dots for the  $T_1$  state at the planar  $T_1$  minimum ( $T_{1,min}^*$ ) are quite separated from the rest of the  $T_1$  cluster. A probable reason is that this geometry is quite similar to the Frank-Condon (FC) point, except for a slight elongation of the C=C bond. In particular, in contrast to the other excited state minima, the C-S bond distance is relatively short. Therefore, it is easier for the electron hole created by UV

excitation on the S atom to redistribute partially on the neighbouring atoms. Then, the 2p binding energy decreases.

The opposite is true for the dots of the  $S_2$  state at the planar  $S_2$  minimum ( $S_{2,\min}^*$ ). Indeed, among the planar geometries, this is the one with the largest C-S bond distance, so that the hole is more likely to localize on the S atom.

Note that, although these points shift away from their clusters, the shift always correlates with the electron binding energy: the higher the partial charge on the S atom, the higher the ionization potential.

## 6 Pulse energy scans

Power-dependent scans were performed for x-ray only probing (Fig. S10) to assure that the x-ray induced photoelectron signal is not saturated. The resulting x-ray pulse energy distribution used in the experiment is shown in Fig. 10c. Similarly, UV-power scans were performed (Fig. S10) to avoid UV induced saturation effects. Here, the absolute of the total difference intensity is plotted as a function of UV pulse energy. The resulting pulse energy histogram with energies in the linear excitation regime is given in Fig. S10d.

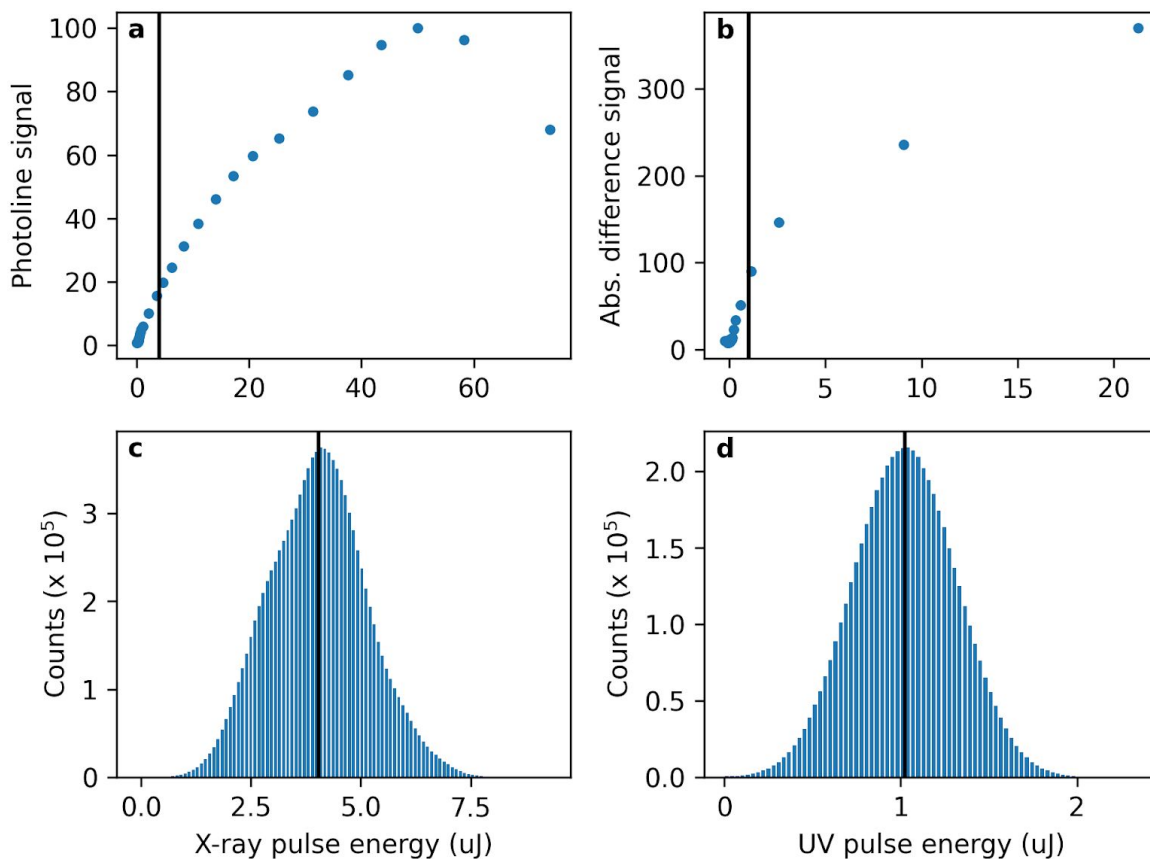


*Figure S10: a: X-ray-only S2p photoelectron signal as a function of x-ray pulse energy. b: Integrated absolute difference signal at S2p photoline as a function of UV pulse energy. c and d: X-ray and UV pulse energy distribution for the experimental data shown in the paper. The vertical black lines mark the centre of gravity of the distributions. They are also inserted in a & b for comparison to the pulse energy scans.*

## 7 Data handling

The data presented covers about 8 million FEL shots. All electron time-of-flight traces have been normalised on FEL pulse energy prior to further processing. As shot-to-shot FEL photon energies are not delivered by FLASH, long term drifts and trends over the FEL pulse train have been tracked with the sulphur 2p photoline itself and corrected via self-referencing the photoline using the following procedure.

In order to determine the photoline position in the time-of-flight spectra better, a number of 200 consecutive pulse trains (20s of data, 50 pulses per train) were averaged pulse-wise. The resulting 50 spectra were fitted with a Gaussian function within a 200 ns window around the expected photoline position. However, only every second shot can be used to evaluate the influence of the FEL on the spectrum as the other half was additionally influenced by the UV pump. The trend over pulse train of the remaining 25 values is fitted with a second order polynomial. The resulting curve is used to shift the original 10,000 raw spectra. To track not only the trends over the pulse trains but also long term shifts, the overall mean of the photoline position of the first of those processed data chunks is set as a global reference. The raw spectra for all data chunks are shifted towards this reference utilizing the (for each chunk determined) pulse train trend of the average spectra.

After that, shot-to-shot difference spectra were calculated and the resulting spectra were binned by delay. The delays were corrected by means of the bunch arrival monitor (BAM) which measures the arrival of the electron bunches and thus gives information on the arrival time jitter of the x-ray pulses<sup>1,2</sup>. The delay binning was chosen in such a way that all bins have similar statistics (~73,000 shot pairs per bin). In combination with the delay correction via BAM, this allows a finer binning for delays close to time-zero than experimentally set.

## References

1. Schulz, S. *et al.* Femtosecond all-optical synchronization of an X-ray free-electron laser. *Nature Comm.* **6**, 5938 (2015).
2. Savelyev, E. *et al.* Jitter-correction for IR/UV-XUV pump-probe experiments at the FLASH free-electron laser. *New J. Phys.* **19**, 043009 (2017).
3. Kruit, P. & Read, F. H. Magnetic field paralleliser for  $2\pi$  electron-spectrometer and electron-image magnifier. *J. Phys. E: Sci. Instrum.* **16**, 313–324 (1983).
4. Mai, S., Marquetand, P. & González, L. A Static Picture of the Relaxation and Intersystem Crossing Mechanisms of Photoexcited 2-Thiouracil. *J. Phys. Chem. A* **119**, 9524–9533 (2015).

5. Khvorostov, A., Lapinski, L., Rostkowska, H. & Nowak, M. J. UV-Induced Generation of Rare Tautomers of 2-Thiouracils: A Matrix Isolation Study. *J. Phys. Chem. A* **109**, 7700–7707 (2005).
6. Vidal, M. L., Krylov, A. I. & Coriani, S. Dyson orbitals within the fc-CVS-EOM-CCSD framework: theory and application to X-ray photoelectron spectroscopy of ground and excited states. *Phys. Chem. Chem. Phys.* **22**, 2693–2703 (2020).